

Disorder effect on the anisotropic resistivity of phosphorene determined by a tight-binding model

Carlos J. Páez,¹ Kursti DeLello,² Duy Le,² Ana L. C. Pereira,¹ and Eduardo R. Mucciolo²

¹*Faculdade de Ciências Aplicadas, Universidade Estadual de Campinas, 13484-350 Limeira, SP Brazil*

²*Department of Physics, University of Central Florida, Orlando, FL 32816-2385, USA*

In this work we develop a compact multi-orbital tight-binding model for phosphorene that accurately describes states near the main band gap. The model parameters are adjusted using as reference the band structure obtained by a density-functional theory calculation with the hybrid HSE06 functional. We use the optimized tight-binding model to study the effects of disorder on the anisotropic transport properties of phosphorene. In particular, we evaluate how the longitudinal resistivity depends on the lattice orientation for two typical disorder models: dilute scatterers with high potential fluctuation amplitudes, mimicking screened charges in the substrate, and dense scatterers with lower amplitudes, simulating weakly bounded adsorbates. We show that the intrinsic anisotropy associated to the band structure of this material, although sensitive to the type and intensity of the disorder, is robust.

PACS numbers: 71.20.nr, 73.63.-b, 71.10.Fd

I. INTRODUCTION

Two-dimensional (2D) materials formed by a few atomic layers are likely to be featured in high-performing electronic devices in the near future, thanks to their high charge mobility, strong gating capabilities, and other unusual properties. For nearly a decade, the focus was primarily on graphene,¹ but its use in transistors as a substitute for silicon has many limitations; in particular, the absence of a bandgap.² The focus now has shifted to others 2D material. Among these, monolayer black phosphorus, known as phosphorene, is particularly attractive. Phosphorene has high charge mobility (typically $100 - 1000 \text{ cm}^2\text{V}^{-1}\text{s}^{-1}$),^{3,4} its band gap spans a wide range in the visible spectrum, and presents a strong in-plane anisotropy.⁵⁻⁷

Current methods for calculating the band structure and optical and electronic properties of phosphorene include density functional theory (DFT). Attempts at studying the electronic properties of phosphorene have also been made using a self-consistent pseudopotential approach.⁸⁻¹¹ Those approaches are highly successful in predicting the overall trend of the band structure, but they can be computationally expensive for calculating the transport properties.

Previous works dealing with phosphorene focused on obtaining the optical and electronic properties using tight-binding models with only one p_z orbital per atom.¹²⁻¹⁵ However, these simple models do not capture the anisotropy in the electronic and optical properties accurately.

Differently from graphene, the atomic layers in phosphorene are not perfectly flat; instead, phosphorene has a puckered surface due to the sp^3 hybridization. Thus, for an accurate description of the electronic properties including the anisotropy, both p and s orbitals have to be taken into account. Recently, a tight-binding model has been developed which includes nearest and next-nearest

neighbor interactions.¹⁶ While this model offers only a qualitative view of the behavior of the band structure, it also provides reasonable predictions in agreement with experimental results, and can serve as a good starting point for our model.

In this work, we develop an effective tight-binding model for phosphorene through a optimization procedure of the tight-binding parameters. The tight-binding model is built with an orthogonal basis composed of all $3s$ and $3p$ orbitals of phosphorus. It reproduces very accurately the energy bands and reasonably well the orbital compositions near the extremes of the conduction and valence bands, as obtained by DFT calculations based on the hybrid HSE06 functional,^{17,18} referred herein as DFT-HSE06.

Using this optimized tight-binding model, we calculate the linear conductance of phosphorene for two different lattice orientation (zigzag and armchair) in the presence of background potential fluctuations that mimic disorder. Our aim is to investigate the in-plane anisotropy in the transport when in presence of disorder. We consider two limits of the Gaussian-correlated potential fluctuations: low amplitudes with high density, and high amplitude with low density. In both regimes, we find that the intrinsic anisotropy due to the electronic structure is manifest in the resistivity of phosphorene.

Phosphorene samples are shown to be very sensitive to the environment,¹⁹⁻²¹ therefore, the role of disorder represents an important issue, with both theoretical and practical relevances. First-principle studies of the effects of vacancies,²² substitutional atoms,²³ oxidation,²⁴ and impurities²⁵ have been only carried out so far for small systems due to the high computational cost. However, the computation of transport properties in particular requires the carriers to be in the proper dynamical regime (diffusive in most cases), which in turn can only be simulated in large enough samples. Therefore, the influence of disorder on the transport properties of phosphorene is not yet settled.

The remaining of the paper is organized as follows. In Sec. II, the optimization procedure used in our tight-binding model to calculate the band structure is presented. In Sec. III, we compare the band structure obtained from the DFT-HSE06 and from our optimized tight-binding model. In Sec. IV, the band structure around the high-symmetry Γ -point is analyzed, allowing us to obtain accurate values for the effective masses in zigzag and armchair directions. In Sec. V, we study the effects of disorder on the transport properties of phosphorene, specially on the anisotropic resistivity. Finally, in Sec. VI, we draw our conclusions. The main text is supplemented by Appendix A containing technical aspects of the simplified LCAO method calculations.

II. MODEL

The crystal structure of monolayer phosphorene is illustrated in Fig. 1a. While graphene is planar atomic layer of carbon, phosphorene is a non-planar layer of phosphorus atoms, forming a puckered structure where atoms are located on two parallel planes. As a result, phosphorene has an anisotropic crystal structure.

Figure 1b shows the projection of the phosphorene crystal onto the a plane. The rectangular area indicates a unit cell, which contains four atoms labeled A, B, A' and B'. Their positions in the unit cell are: $\tau_A = (uc_0, 0, vb_0)$, $\tau_B = ((1/2 - u)c_0, a_0/2, vb_0)$, $\tau_{A'} = -\tau_A$ and $\tau_{B'} = -\tau_B$, where $a_0 = 3.314\text{\AA}$, $c_0 = 4.376\text{\AA}$, and $b_0 = 10.48\text{\AA}$,

are the corresponding lattice constants in y (zigzag), x (armchair) and z directions.^{8,16} Here, $u = 0.08056$ and $v = 0.10168$ are dimensionless crystal structure parameters. From these atom locations, we can define the first eight lattice displacement vectors in Table I.

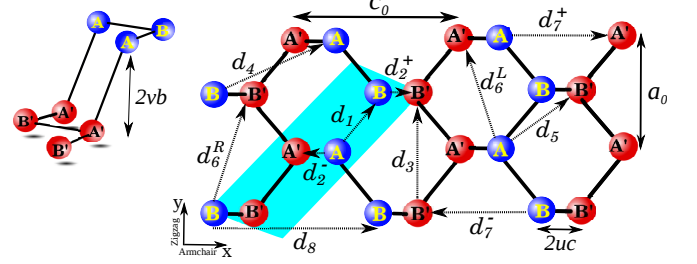


FIG. 1. (Color online)(a) Red (blue) circles represent phosphorus atoms in the lower (upper) layer. (b) Projection of the phosphorene crystal structure onto a two-dimensional plane. The rectangular area indicates the unit cell, which contains four phosphorus atoms. Zigzag and armchair edges are indicated.

We include the $3s$ and $3p_{x,y,z}$ electrons in the partially filled atomic shells and neglect any spin-orbit coupling since phosphorus is a low- Z element.²⁶ The effective Hamiltonian is represented as the following 16×16 matrix within the basis $(A_s, A_{p_x}, A_{p_y}, A_{p_z}, B_s, B_{p_x}, B_{p_y}, B_{p_z}, A'_s, A'_{p_x}, A'_{p_y}, A'_{p_z}, B'_s, B'_{p_x}, B'_{p_y}, B'_{p_z})$:

$$H_{\text{mono}}(\mathbf{k}) = \begin{bmatrix} T_0 + T_3 + T_8 & T_1 + {}^tT_4^* & T_2^- + T_6^L + T_7^+ & T_5 \\ {}^tT_1^* + T_4 & T_0 + T_3 + T_8 & T_5 & T_2^+ + T_6^R + T_7^- \\ {}^tT_2^{-*} + {}^tT_6^{L*} + {}^tT_7^{+*} & {}^tT_5^* & T_0 + T_3 + T_8 & {}^tT_1^* + T_4 \\ {}^tT_5^* & {}^tT_2^{+*} + {}^tT_6^{R*} + {}^tT_7^{-*} & T_1 + {}^tT_4^* & T_0 + T_3 + T_8 \end{bmatrix}. \quad (1)$$

We take into account up to eighth nearest neighbor couplings (see Fig. 1b) through eight 4×4 matrices referred to as T_i , within the $\{|m\rangle\}$ basis of atomic shells. Here, the index m represents s , p_x , p_y , and p_z orbitals. The interatomic matrix elements $T_i^{m,m'}(\mathbf{k})$ are given by the expression

$$T_i^{m,m'}(\mathbf{k}) = t_{mm'}^i \sum_{j=1}^N e^{i(\mathbf{R}'_j + \mathbf{r}'_i - \mathbf{r}_l) \cdot \mathbf{k}}, \quad (2)$$

where N is the number of unit cells, \mathbf{R}_j denotes the position of the j th unit cell of the Bravais lattice, and \mathbf{r}_l is the position of the atom l within the unit cell. In this case, we sum only over the adjacent unit cells j which contain the atoms l , with the displacement vector magnitude given by $|\mathbf{R}'_j + \mathbf{r}'_i - \mathbf{r}_l| = |\mathbf{d}_i|$. The lattice displacement vector are provided in Table I. The hopping amplitudes $t_{mm'}^i$ are initially written in terms of Slater-Koster (SK)

Order	Distances (\AA)
$\mathbf{d}_1 = \tau_B - \tau_A$	2.224
$\mathbf{d}_2^+ = \tau_{B'} + \mathbf{a} + \mathbf{c} - \tau_B$, $\mathbf{d}_2^- = \tau_{A'} - \tau_A$	2.244
$\mathbf{d}_3 = \mathbf{a}$	3.314
$\mathbf{d}_4 = \tau_A + \mathbf{a} + \mathbf{c} - \tau_B$	3.334
$\mathbf{d}_5 = \tau_{B'} + \mathbf{a} + \mathbf{c} - \tau_A$	3.475
$\mathbf{d}_6^R = \tau_{B'} + 2\mathbf{a} + \mathbf{c} - \tau_B$, $\mathbf{d}_6^L = \mathbf{d}_6^R - 4uc$	4.002
$\mathbf{d}_7^+ = \mathbf{d}_2^- + \mathbf{c}$, $\mathbf{d}_7^- = \mathbf{d}_2^+ - \mathbf{c}$	4.245
$\mathbf{d}_8 = \mathbf{c}$	4.376

TABLE I. Intersite distances. Following Ref. 8, the lattice vectors are defined as $\mathbf{a} = (0, a_0, 0)$ and $\mathbf{c} = (c_0, 0, 0)$.

parameters.²⁷

A. Reference Density Function Band Structure

In order to optimize the tight-binding model, we employ a DFT calculation to generate a reference band structure for phosphorene. We use the supercell method with a plane-wave basis set at a cutoff energy of 500 eV and the projector-augmented wave technique,^{28,29} as implemented in the Vienna *ab-initio* Simulation Package (VASP).^{30,31} We use the hybrid HSE06^{17,18} functional for the exchange-correlation of the electrons. The supercell consists of a unit cell of monolayer black phosphorus with experimental lattice parameters, bond lengths, and bond angles³² and a vacuum of 15 Å. The Brillouin zone is sampled over a $(9 \times 12 \times 1)$ k -point mesh for a self-consistent calculation. The electronic band structure along high-symmetry directions is calculated with a finer mesh of k -points and then projected onto every orbital of each atom to resolve the symmetry character of the corresponding wavefunctions (i.e., their l and m numbers). The band structure obtained in our DFT-HSE06 calculations shows that single layer black phosphorus is a direct band gap material with a band gap (E_g) of 1.1 eV, which is quite close to the experimentally measured values so far (of 1.0 and 1.55 eV).^{4,33–35}

B. Optimization of hopping parameters

Our tight-binding model Hamiltonian has 16×16 hopping amplitudes $t_{mm'}^i$. Due to symmetry, we only need to calculate 58 of these elements. These parameters are optimized to reproduce the main characteristics of the energy bands near the main gap, as obtained from DFT-HSE06 calculations. The route to approximate the band structure is the following:

- Step 1: Following Slater and Koster,²⁷ we initially constructed the tight-binding Hamiltonian for phosphorous $3s$, $3p_x$, $3p_y$ and $3p_z$ orbitals (see Eq. (1)). Under this scheme, the hopping amplitudes $t_{mm'}^i$ are defined at first as a function of Slater-Koster parameters ($V_{ss\sigma}$, $V_{sp\sigma}$, $V_{pp\sigma}$ and $V_{pp\pi}$), as described in detail in the Appendix A. By diagonalizing $H_{\text{mono}}(\mathbf{k})$ for this first choice of hopping parameters, we obtain the band structure of monolayer phosphorene, as shown in Fig. 2, together with the band structure for the DFT-HSE06 calculations. Unfortunately, it is clear from Fig. 2 that this simple model fails to resolve finer details in the band structure, which are important for electronic transport calculations. Although the results obtained from the SK parameters are largely inaccurate when compared with DFT-HSE06 calculations, they serve as a useful starting point to optimize the tight-binding parameters, using the method of least squares as described in the next two steps.
- Step 2: We then generate several different sets of

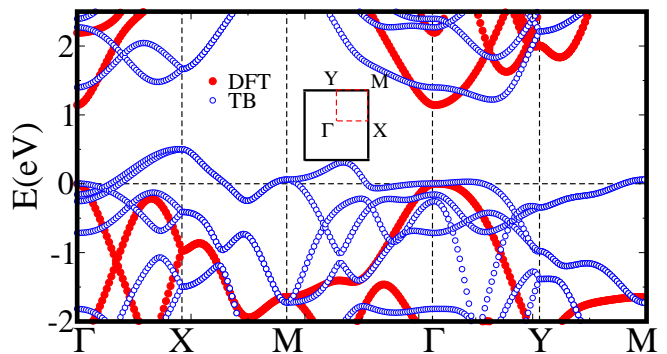


FIG. 2. (Color online) Comparison between the band structures obtained with the DFT-HSE06 (red squares) and with Slater-Koster tight-binding model (blue circles)

parameters $t_{mm'}^i$ from the initial hopping amplitudes obtained in step 1. Each of these sets is generated by adding to the initial hoppings a random amplitude δV , taken from a uniform distribution over the interval $[-1, 1]$ meV. Following this, we take here 1000 slightly different parameter sets.

- Step 3: For each of the new parameter sets, we choose the same number of representative k -points and calculate, by diagonalization of $H_{\text{mono}}(\mathbf{k})$, the corresponding band energies $E_n(k)$, where n is the band index. We find the best tight-binding set of parameters among the 1000 generated by choosing the set that gives the lowest possible χ^2 function, where χ^2 is just a sum of weighted squared residuals,³⁶ namely,

$$\chi^2 = \sum_{i=C,V} \sum_{j=1}^N \frac{[E_i^{TB}(j) - E_i^{DFT}(j)]^2}{\sigma_j^2}, \quad (3)$$

where j labels the k points and i labels the lowest conduction (C) and highest valence (V) energy bands. To improve the approximation we give a larger weight $\sigma_j = 1$ to points $(k, E_n(k))$ near the Γ point. In addition, we take a larger concentration of points around Γ to reproduce the effective band masses around this high-symmetry point.

- Step 4: Steps 2 and 3 are iteratively repeated (restarting step 2 each time with the best set selected in step 3) until χ^2 becomes smaller than 1 meV². When this convergence criterion is satisfied, the optimized tight-binding parameters are obtained.

Table II presents the best fitting parameters we obtained using the the optimization procedure described above. It is important to emphasize that these parameters correspond to the single layer black phosphorus, and, although they would be modified for other phosphorene allotropes,³⁷ the same optimization procedure to find the best tight-binding parameters can be applied.

i	t_{ss}^i	t_{sx}^i	t_{sy}^i	t_{sz}^i	t_{xx}^i	t_{xy}^i	t_{xz}^i	t_{yy}^i	t_{yz}^i	t_{zz}^i
1	1.402	-0.316	0.247		1.236	2.665		6.083		-1.770
2	-1.418	-1.173		-0.775	-1.541		-0.841	-5.809		2.170
3	0.349		-0.100		0.079			0.568		0.042
4	-0.239	0.300	-0.639		0.599	0.904		1.006		0.753
5	-0.255	-0.303	-0.246	-0.180	0.328	-0.038	0.166	0.654	0.659	0.096
6	-0.123	0.259	-0.072	0.100	0.063	0.305	-0.055	-0.206	-0.683	-0.313
7	-0.221	-0.146		-0.128	0.349		-0.077	-0.018		0.628
8	0.266	-0.260			-0.588			0.147		-0.037

TABLE II. Tight-binding model parameters obtained by optimization. The values are given in units of eV.

III. BAND STRUCTURE AND ORBITAL CONTRIBUTION

In Fig. 3 we show a comparison between the band structures for a single-layer phosphorene obtained with DFT-HSE06 and that obtained from the optimized tight-binding model described in the previous section. The optimized tight-binding model is in good agreement with the DFT-HSE06 results and is quite accurate near the minimum of the conduction band and the maximum of the valence band (see Fig. 3a). These are the most important regions of the spectrum as far as electronic transport is concerned and therefore accuracy here is fundamental for obtaining realistic predictions for transport properties.

We point out that this level of accuracy is missing in previous studies, where simpler tight-binding Hamiltonians were employed; for example, in models based on a single p orbital.^{9,12–15,38} In those simpler models the bands near the main energy gap have a large discrepancy with respect to the DFT results (the green continuous line in Fig. 3b represents the tight-binding results considering only the p_z orbital). For most of these previous studies, the focus was in describing accurately only the main energy gap of the band structure at the Γ point. In contrast, our optimized tight-binding model, in addition to capturing the energy gap, is able to describe the bands structure in the $\Gamma \rightarrow Y$ and $\Gamma \rightarrow X$ and $\Gamma \rightarrow M$ directions with high accuracy, thus allowing us to properly study the effects of anisotropy on transport properties.

Tight-binding methods employing orbitals $sp^{3,16}$ and $sp^3d^{5,39}$ have been developed including up to second nearest neighbors. Those studies show a clear deviation with respect to DFT results. A description of the electronic structure of phosphorene supported by the Wannier functions formalism has also been performed.⁴⁰ This study was successful in achieving a notable accuracy in the band structure of phosphorene, but the computational cost would be too heavy for studying electronic transport, where very large real-space lattices are required.

In Fig. 4 we show a comparison between the main orbital composition obtained from DFT-HSE06 (Fig. 4a) and from the optimized tight-binding model (Fig. 4b) near the valence band maximum and the conduction

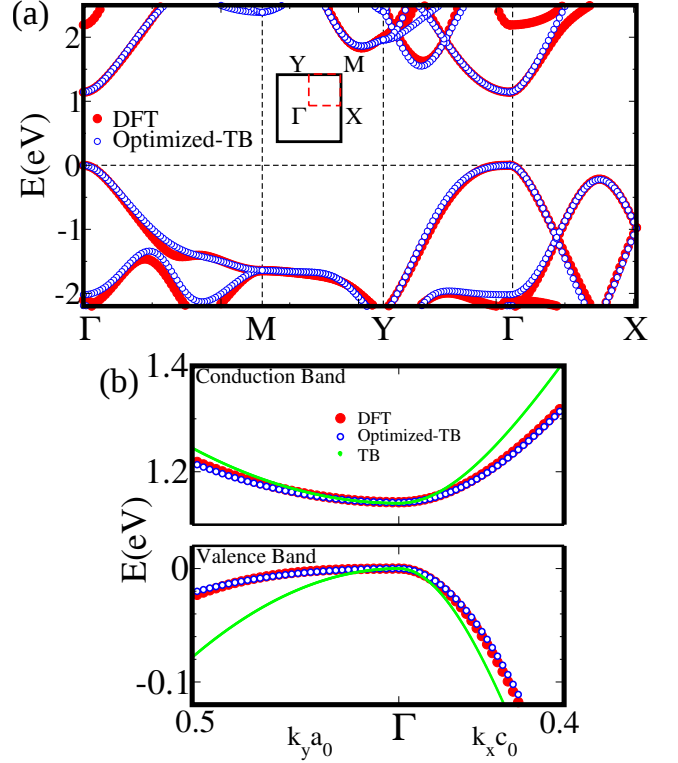


FIG. 3. (Color online) (a) Comparison between the band structures obtained with DFT-HSE06 (red squares) and with the optimized tight-binding model (blue circles). (b) Zoom around the Γ point, showing that the optimized model accurately reproduces the valence and conduction bands from DFT near the gap region. The green continuous line represents the tight-binding results considering only the p_z orbital.

band minimum. Around the Γ point, it can be seen that the main orbital contribution to both bands comes from the p_z orbitals (about 90%). The orbital contributions around the high-symmetry points M , X , Y , and Γ from the optimized tight-binding model show a qualitatively correct composition of the orbitals for both conduction and valence bands when compared with the DFT-HSE06 results. In particular, the composition of the conduction

band shows non-negligible contributions from s , p_x , p_y and p_z orbitals.

IV. ANISOTROPY

Figure 5a shows the dispersion of the valence and conduction bands $E(\mathbf{k})$ around the Γ point obtained numerically by diagonalizing the tight-binding Hamiltonian in Eq. (1). Both bands are clearly anisotropic, as it can be seen in the top and bottom contours. One can see that the valence band near the Γ point is flatter along the k_y direction than along the k_x direction, implying that the hole carriers moving along the zigzag direction are heavier than in the armchair direction. A similar behavior is also observed for the dispersion of conduction band. Strong anisotropy for both electron and hole carriers was observed experimentally in multilayer phosphorene.^{5,41} The different effective masses of the valence and conduction bands along the armchair and zigzag directions is consistent with the in-plane anisotropy reported in several transport experiments.^{6,35,42} In this paper we make this connection quantitative.

The anisotropy can be further identified directly from the anisotropic effective masses as shown in Fig. 5b. From our tight-binding band structure we extract the effective masses for the electrons and holes through the expression $m^* = \hbar^2 \left(\frac{\partial^2 E}{\partial k^2} \right)^{-1}$. The resulting effective masses at Γ point along the armchair direction are $m_{ac}^{*v} = -0.1678m_e$ and $m_{ac}^{*c} = 0.1990m_e$ for holes and electrons respectively. Here, m_e is the free electron mass. The effective masses along the zigzag direction are much heavier than armchair direction: $m_{zz}^{*v} = -5.3525m_e$ and $m_{zz}^{*c} = 0.7527m_e$ for holes and electrons respectively. These values are also in close agreement with other DFT calculations.³³ We note that the single-orbital (p_z) tight-binding method (see green line in in Fig. 2c) cannot accurately capture this effective mass anisotropy.

V. ELECTRONIC PROPERTIES APPROACH: ANISOTROPIC RESISTIVITY

A. Hamiltonian in real space

Numerical studies of electronic transport in 2D materials have to strike a compromise between the model complexity and the length scales that can be investigated. Complex models requiring many basis states per unit cell can only be used to investigate small systems, where the diffusive regime common to experiments cannot be probed. Because of their relative simplicity and small basis state sets, the use of heuristic tight-binding models has grown in interest in the last decade.^{13,39} Very large systems can be studied with these models, sometimes involving over a billion atoms,⁴³ in contrast to *ab initio* approaches. When the length scales associated to

charge carrier scattering involve more than a few lattice spacings, tight-binding models are the only practical choice. We study transport properties of phosphorene starting from our optimized tight-binding Hamiltonian in k -space, Eq. (1). The real-space tight-binding Hamiltonian used in the numerical calculations, denoted by H includes nearest-neighbor hopping terms (within the same unit cell), as well as next-to-nearest-neighbor ones (between adjacent cells), as discussed in Sec. II. Using second quantization, the real-space Hamiltonian can be written as

$$H = \sum_{i=1}^{\mathcal{N}} \sum_{\alpha} \left(\varepsilon_{\alpha}^i c_{\alpha}^{i\dagger} c_{\alpha}^i + \sum_j \sum_{\beta} t_{\alpha,\beta}^j c_{\alpha}^{i\dagger} c_{\beta}^j \right) + \text{H.c.}, \quad (4)$$

where i runs over the \mathcal{N} lattice sites, j runs over the eight neighboring sites of i and α and β run over s and p orbitals. Here, $\varepsilon_s^i = -17.10$ eV and $\varepsilon_p^i = -8.33$ eV are the energy levels of $3s$ and $3p$ orbitals of phosphorus, respectively.⁴⁴ $t_{\alpha,\beta}^j$ is the hopping integral between the i th and its j th neighbor, and c_{α}^i ($c_{\alpha}^{i\dagger}$) is the annihilation (creation) operator of electrons at orbital α on the site i . The different hopping and on-site terms can be visualized in Fig. 1b.

Although we use a relatively simple Hamiltonian to describe phosphorene, it not only captures the physics qualitatively well, but is also quantitatively approximately correct. This is because, in the absence of disorder, both the energy bands and the wavefunctions near the main gap closely resemble those calculated from an accurate *ab initio* theory. Nevertheless, we emphasize that the choice of tight-binding parameters is not unique and not yet fully settled, with several different parameter sets proposed in the literature.^{13,39}

B. Transport calculations

Our calculations of the two-terminal linear conductance follow the well-established Caroli formula,⁴⁵

$$\mathcal{T}(E) = \text{Tr} [\Gamma_p G^r \Gamma_q G^a], \quad (5)$$

which relates the transmission probability (transmittance) $\mathcal{T}(E)$ at a fixed carrier energy E to the Green's functions G^r and $G^a = (G^r)^\dagger$ of the sample when coupled to source (p) and drain (q) contacts (represented by shadow areas in in Fig. 6). The trace indicates a sum over all transverse channels (or, equivalently, over all atomic sites at the sample-electrode contact region). The matrices $\Gamma_{p,q}$ represent the imaginary part of the self-energy due to the coupling to the electrodes, $\Gamma_{p(q)} = i[\Sigma_{p(q)} - \Sigma_{p(q)}^\dagger]$. The Green's functions are obtained by a recursive technique where the sample is split into atomic transverse slices.⁴⁶ We assume that the electrodes are identical semi-infinite phosphorene strips with no disorder; the strip Green's function, which is a fundamental

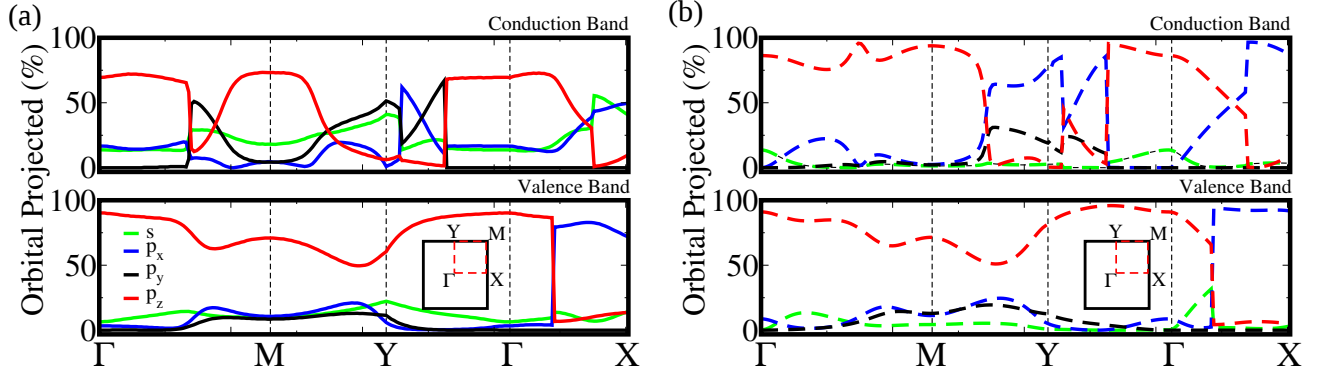


FIG. 4. (Color online) (a) Orbital-projected band structure obtained with DFT-HSE06. (b) Orbital-projected band structure obtained with the optimized tight-binding model. The contribution of each orbital is shown by color: s (green), p_x (blue), p_y (black) and p_z (red).

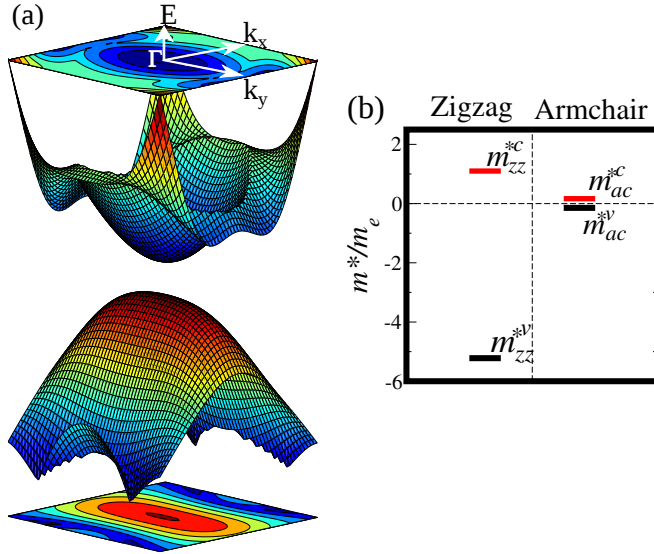


FIG. 5. (a) Three-dimensional contour plot of the valence and conduction bands around the Γ point. (b) Effective masses along armchair and zigzag directions. m^{*c} (in red) and m^{*v} (in black) are the effective masses for the conduction and valence bands, respectively, making evident the anisotropy for both bands.

ingredient in the recursive technique, is obtained numerically using a standard decimation method.⁴⁷

A schematic representation of the system contact-sample-contact is shown in Fig. 6, where L and W are the length and the width of the phosphorene sample considered. M and N indicated in the figure are the number of unit cells in armchair and zigzag directions, respectively. Therefore, for transport along the armchair direction, as is the case represented in Fig. 6, $L = Mc_0$ and $W = Na_0$. If the transport is calculate along the zigzag direction, then $L = Na_0$ and $W = Mc_0$.

Within the Landauer-Büttiker formalism, the linear

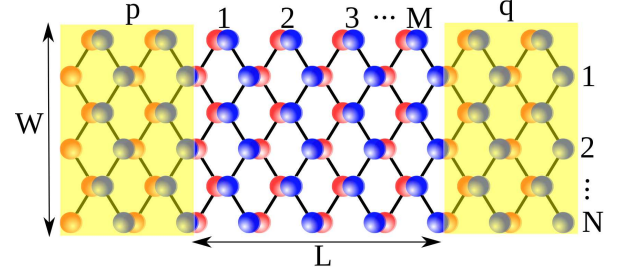


FIG. 6. (Color online) Schematic representation of a phosphorene sample of length L and width W , and the corresponding number (M and N) of unit cells in the armchair and zigzag directions. The shadow areas represent the left (p) and right (q) semi-infinite contacts.

conductance $\mathcal{G}(E)$ at a given energy E is directly related to the transmission function $\mathcal{T}(E)$ between the contacts as

$$\mathcal{G}(E) = \mathcal{G}_0 \mathcal{T}(E), \quad (6)$$

where $\mathcal{G}_0 = 2e^2/h$. The linear resistance follows straightforwardly from $R = 1/\mathcal{G} = R_0/\mathcal{T}$, where $R_0 = 1/\mathcal{G}_0 = 12.5 \text{ K}\Omega$. The resistivity is obtained as usual, namely, $\rho = RW/L$.

In experiments, it is the carrier density n rather than the carrier energy E that can be controlled by a back gate. Thus, in order to explore how the resistivity ρ behaves as a function of disorder strength, we perform the calculations at fixed values of n . For a given realization of disorder, the latter is obtained through the relation

$$n(E) = \frac{1}{A} \int_{E_0}^E dE' \nu(E'), \quad (7)$$

where $A = WL$ is the sheet area and E_0 is a reference energy (either the top of the valence band or the bottom of the conduction band). Note that in the conduction

band, $E > E_0$ and therefore the integral is over positive energies (electrons), while in the valence band, $E < E_0$ and the integral is over negative energies (holes). ν is the global density of states, which can be readily obtained from the energy dependence of the scattering matrix S ,

$$\nu(E) = -\frac{i}{2\pi} \text{Tr} \left(S^\dagger \frac{\partial S}{\partial E} \right). \quad (8)$$

The scattering matrix S is evaluated in terms of the retarded Green's functions G^r ,^{46,48}

$$S_{ab}(E) = -\delta_{ab} + i\hbar \frac{\sqrt{v_a v_b}}{a_0} \sum_i \sum_j \chi_a^*(i) G^r(i, j) \chi_b(j), \quad (9)$$

where i and j run over the sites at the contacts p and q , where the propagating channels a and b are defined, respectively. Here a_0 is the lattice constant and $v_{a,b}$ and $\chi_{a,b}$ are, respectively, the longitudinal propagation velocity and the transverse wavefunction in the propagating channel. We obtain $v_{a,b}$ and $\chi_{a,b}$ from the eigenvalues and eigenfunctions of the $\Gamma_{p(q)}$ matrices,

$$\Gamma_{p(q)}(i, j) = \sum_a \chi_a(i) \frac{\hbar v_a}{a_0} \chi_a^*(j). \quad (10)$$

C. Disorder effects over the anisotropy

We studied the disorder effects by using the optimized tight-binding method previously described, which allows for very efficient large-scale calculations of linear transport properties. To model disorder, a superposition of Gaussian potential fluctuations is added to the Hamiltonian in Eq. (4) as a diagonal term,⁴⁹

$$U(\mathbf{r}_i) = \sum_{k=1}^{N_{\text{imp}}} U_k e^{-|\mathbf{r}_i - \mathbf{R}_k|^2 / 2\xi^2}, \quad (11)$$

where r_i denotes a lattice site. The N_{imp} Gaussian scatterers have a width ξ , are located at random sites $\{\mathbf{R}_k\}_{k=1, N_{\text{imp}}}$ drawn uniformly and have amplitudes $\{U_k\}_{k=1, N_{\text{imp}}}$ taken from a flat distribution in the interval $[-\delta U/2, \delta U/2]$. Let $n_{\text{imp}} = N_{\text{imp}}/\mathcal{N}$ denote the density of scatterers. Motivated by the two prevailing scattering mechanisms in phosphorene transistors, we consider two extreme cases: (i) dense disorder ($n_{\text{imp}} = 1\%$) with low amplitude of the Gaussian potential fluctuations ($0.03 \leq \delta U \leq 0.14$ eV); and (ii) dilute disorder ($n_{\text{imp}} = 0.1\%$), with higher amplitudes of the Gaussian potential ($0.2 \leq \delta U \leq 2$ eV). Case (i) models contaminants such as water, which attach to phosphorene by weak van der Waals interactions (therefore the low amplitudes). Case (ii) models background potential inhomogeneities like those caused by screened charges in the substrate. Notice that although the Gaussian potential we consider is short-range on the system-size

scale (correlation-length $\xi = 1.5a_0$), it varies smoothly on the atomic scale, corresponding to an effective disorder which mimics the effect of screened charges from the substrate.^{46,49}

In Fig. 7 we show the average resistance as a function of length of the system for the disorder case (i). Different panels correspond to the resistance along armchair or zigzag directions, for conduction and valence bands, as indicated. In each one, we show curves for different disorder potential amplitude δU . The range of the Gaussian potential considered is $\xi = 1.5a_0$ for all of them. The average is computed over 500 disorder configurations and for a carrier density $n = 3 \times 10^{12} \text{ cm}^{-2}$, which brings the Fermi energy close to the bottom (top) of the conduction (valence) band. We present similar data for the disorder case (ii) in Fig. 8.

At zero temperature, the resistance strongly fluctuates from one realization to another, which is typical for a coherent quasi-one-dimensional system. However, it is clear from Figs. 7 and 8 that the linear behavior, which is characteristic from a diffusive regime, is kept for longer lengths for the armchair direction than in the zigzag direction, particularly when the amplitude δU of the disorder potential is increased. For longer lengths, the average resistance increases much more rapidly with length, marking the onset of strong localization. For both the conduction and valence regions, we have found that a strong localization regime sets in with increasing L , with an exponential increase of the resistance.

In the diffusive regime, we can extract the resistivity ρ for different disorder amplitudes δU from the linear fittings indicated in Figs. 7 and 8. The inset in each graph shows the resistivity as function of δU , where we find a very good match to a quadratic dependence for all cases. The resulting quadratic fitting for the resistivity as a function of δU is indicated in the top right of each graph in Figs. 7 and 8. ρ_{ZZ} and ρ_{AC} indicates the resistivity along the zigzag and armchair directions, respectively.

Using classical kinetic transport theory, the resistivity ρ can be related to the effective masses m^* and the mean scattering time τ through: $\rho = m^* / \tau n q^2$, where n and q are the density and the charge of the carriers, respectively. Even though an expression for τ is not exactly known, it can be estimated in perturbation theory to be inversely proportional to δU^2 . Thus, the quadratic dependence on δU we observe in the data can be attributed to τ .

It is reasonable to expect the resistivity to be anisotropic, considering the anisotropy in the effective masses. If the classical kinetic transport theory is applicable here, we would expect $\rho_{ZZ}/\rho_{AC} = m_{ZZ}^*/m_{AC}^*$. In Table III we summarize our results for the ratios of resistivities ρ_{ZZ}/ρ_{AC} for the two disorder cases analyzed and also for two sample widths: a thinner one, with 60 unit cells in width and a larger one, with 150 (where all other parameters are kept constant). These results should be compared with the ratios of effective masses obtained from the ordered phosphorene system band struc-

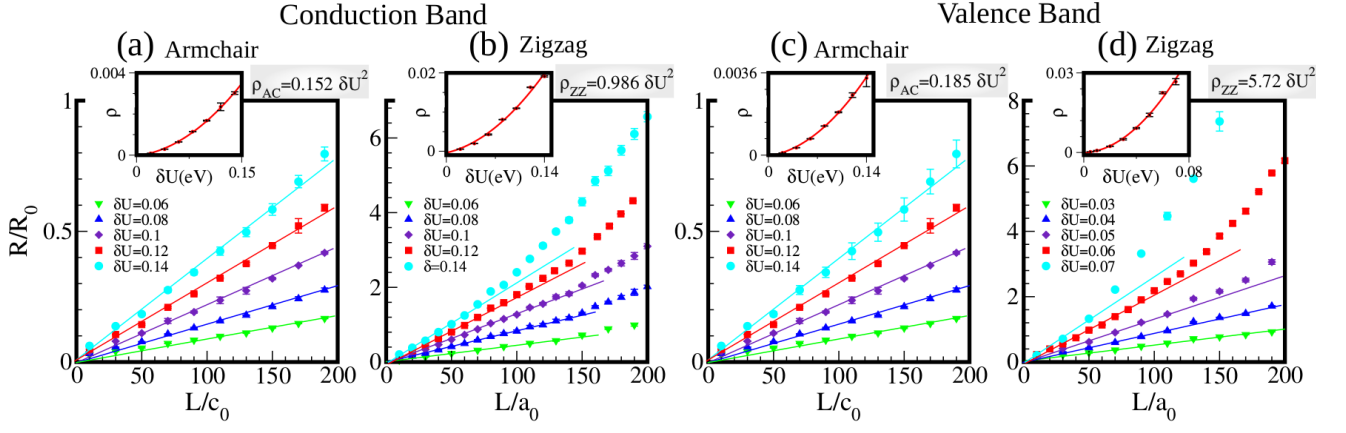


FIG. 7. (Color online) Average resistance as a function of length L for disorder case (i), corresponding to a dense concentration of scatterers ($n_{\text{imp}} = 1\%$), with low disorder amplitudes δU . Continuous lines are linear fittings used to extract the resistivity in the diffusive regime of the data for each curve. Insets: Resistivity as a function of disorder amplitudes δU , showing a quadratic dependence.

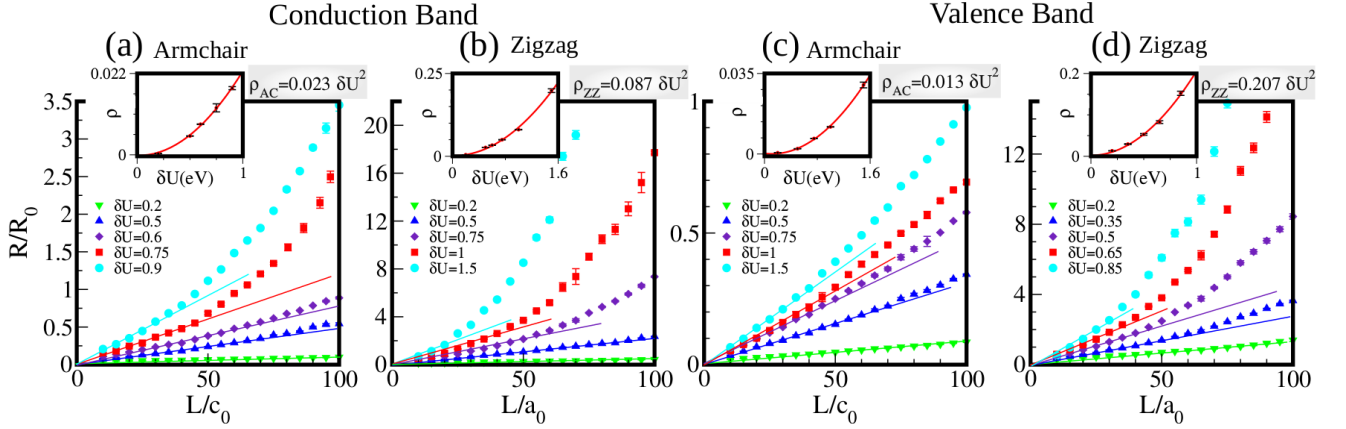


FIG. 8. (Color online) Average resistance as a function of length L for disorder case (ii), corresponding to a dilute concentration of scatterers ($n_{\text{imp}} = 0.1\%$), with high disorder amplitudes δU . Continuous lines are linear fittings used to extract the resistivity in the diffusive regime of the data for each curve. Insets: Resistivity as a function of disorder amplitudes δU , showing a quadratic dependence.

ture (see Sec. IV): $m_{ZZ}^*/m_{AC}^* = 6.6$ for the conduction and $m_{ZZ}^*/m_{AC}^* = 39.4$ for the valence band. Our intention is to observe how different densities and amplitudes of disorder change anisotropy. First of all, we observe from the results in Table III that increasing the width of the phosphorene sample considered from 60 to 150 unit cells does not change considerably the resistivity ratios, which means that we do not have system size effects masking our results here.

Comparing the two disorder cases considered here, we can conclude from the resistivity ratios in Table III that the higher amplitudes of the disorder in the second case (even considering the 10 times lower concentration of scatterers) cause stronger impact in diminishing the anisotropy when compared to the first case. Nevertheless, in both cases the anisotropy is still evident and in

ratios that would be experimentally detected.

It is helpful to analyze the results in light of the product $\delta U^2 \times n_{\text{imp}}$, considering that in the Boltzmann transport, mobility depends on this product.^{46,49} In our calculations, the impurity density n_{imp} is kept fixed for each disorder case, while δU is varied. For the case with dense disorder and low amplitude (shown in Fig. 7), the value of the product was mostly higher than for the case with dilute disorder and high amplitude (shown in Fig. 8): $\delta U^2 \times n_{\text{imp}}$ varies in the interval $[9 \times 10^{-7}, 2 \times 10^{-4}] \text{eV}^2$ for the former and in the interval $[4 \times 10^{-5}, 4 \times 10^{-3}] \text{eV}^2$ for the latter. This is consistent with the results summarized in Table III, where one can observe the stronger suppression of the anisotropy for the disorder with the higher value of the product $\delta U^2 \times n_{\text{imp}}$. Interestingly, cases with different disorder type but with the same δU^2

$\times n_{imp}$ product values, present the same resistance values in Figs. 7 and 8, confirming the universality related to this product.

	Ordered System	Dense disorder Low amplitude	Dilute disorder High amplitude
	m_{ZZ}^*/m_{AC}^*	ρ_{ZZ}/ρ_{AC}	ρ_{ZZ}/ρ_{AC}
Thinner sample			
Conduction	6.6	6.5 ± 0.1	3.8 ± 0.1
Valence	39.4	31 ± 1	16 ± 1
Larger sample			
Conduction	6.6	6.6 ± 0.1	4.1 ± 0.1
Valence	39.4	32 ± 1	18 ± 1

TABLE III. Ratio between the resistivity along the zigzag and armchair directions ρ_{zz}/ρ_{ac} for dilute and dense disorder cases. Effective mass ratios are $m_{ZZ}^*/m_{AC}^* = 6.6$ and $m_{ZZ}^*/m_{AC}^* = 39.4$ for conduction and valence bands, respectively.

VI. SUMMARY AND CONCLUSION

We have developed a tight-binding model for monolayer phosphorene that accurately describes both conduction and valence band dispersions near the Gamma point and approximates well the band compositions. The additional accuracy came at the expense of introducing s in addition to p orbitals, as well as hopping amplitudes involving eight neighbors in total.

We optimized the model parameters by using as benchmark the electronic structure obtained by density functional theory calculation based on the HSE06 exchange-correlation functional. An excellent match between effective masses near the main band gap and along major symmetry directions was obtained.

Using the optimized tight-binding model and a recursive Green's function technique, we computed the resistivity in the presence of disorder for two relevant situations, which mimic two commons types of disorder in phosphorene: (i) weakly bonded adsorbates (simulated by a dense concentration of scatterers, with low amplitudes of the Gaussian potential fluctuations), and (ii) screened charge traps in the substrate (simulated by a dilute concentration of Gaussian correlated disorder, with higher amplitudes). We found that the band mass anisotropy is strongly manifest in the resistivity for the first disorder case, where the ratio of the resistivity along zigzag and armchair directions matches quite closely the ratio for the corresponding effective masses. The anisotropy is weaker, but still robust, in the second disorder case. Thus, we conclude that the most prevailing types of disorder likely to be found in monolayer phosphorene should not wash away the intrinsic band structure anisotropy of this material. Transport experiments performed with thick films of black phosphorus (which is a

multilayer phosphorene), have already demonstrated intrinsic anisotropy.^{4,7,50,51} Based on our results, we expect a similar behavior for monolayer systems.

ACKNOWLEDGMENTS

CJP and ALCP acknowledge financial support from FAPESP through Grant 2015/12974-5. Part of the numerical simulations were performed at the computational facilities at CENAPAD-SP, UNICAMP and UCF Advanced Research Computing Center. DFT calculations are supported in part by the DOE grant DE-FG02-07ER46354.

Appendix A: Slater-Koster

We develop an effective tight-binding model based on the LCAO method¹⁶ and use DFT calculations as the basis for adjusting the model parameters. We begin with a simplified LCAO model. The hopping amplitudes depend of the transfer integral between two adjacent atoms. The transfer integrals are given by $V_{ll'm}(d) = \eta_{ll'm} \hbar^2 / m_e d^2$, where d is the inter-atomic distance, m_e is the electron rest mass, l and l' are the orbital azimuthal quantum numbers (s, p) of two atoms and m is the common orbital magnetic quantum number (σ, π). $\eta_{ll'm}$ is a dimensionless quantity that depends on the crystal structure. For the simplified model, the parameters employed are: $\eta_{ss\sigma} = -1.40$, $\eta_{sp\sigma} = 1.84$, $\eta_{pp\sigma} = 3.24$, and $\eta_{pp\pi} = -0.81$.⁴⁴

When expressed in momentum space, the tight-binding Hamiltonian is a 16×16 matrix, (see Eq. (1)). Here the elements T_i represent 4×4 matrices. The T_0 matrix on the diagonal expresses the energies of the four atomic sites:

$$T_0 = \begin{bmatrix} \varepsilon_s & 0 & 0 & 0 \\ 0 & \varepsilon_p & 0 & 0 \\ 0 & 0 & \varepsilon_p & 0 \\ 0 & 0 & 0 & \varepsilon_p \end{bmatrix} \quad (A1)$$

Here, $\varepsilon_s = -17.10$ eV and $\varepsilon_p = -8.33$ eV represent the energy levels of the $3s$ and $3p$ orbitals of phosphorus, respectively. The nearest and next-nearest neighbor coupling between atoms are represented by T_1 to T_8 respectively:

$$T_1 = \begin{bmatrix} t_{ss}^{(1)} g_1^+ & t_{sx}^{(1)} g_1^+ & t_{sy}^{(1)} g_1^- & 0 \\ -t_{sx}^{(1)} g_1^+ & t_{xx}^{(1)} g_1^+ & t_{xy}^{(1)} g_1^- & 0 \\ -t_{sy}^{(1)} g_1^- & t_{xy}^{(1)} g_1^- & t_{yy}^{(1)} g_1^+ & 0 \\ 0 & 0 & 0 & t_{zz}^{(1)} g_1^+ \end{bmatrix}, \quad (A2)$$

with

$$g_1^\pm(\mathbf{k}) = e^{i\mathbf{d}_1 \cdot \mathbf{k}} (1 \pm e^{-a \cdot \mathbf{k}}); \quad (A3)$$

$$\mathbf{T}_2^\pm = \begin{bmatrix} t_{ss}^{(2)} g_2^\pm & \pm t_{sx}^{(2)} g_2^\pm & 0 & t_{sz}^{(2)} g_2^\pm \\ \mp t_{sx}^{(2)} g_2^\pm & t_{xx}^{(2)} g_2^\pm & 0 & \pm t_{xz}^{(2)} g_2^\pm \\ 0 & 0 & t_{yy}^{(2)} g_2^\pm & 0 \\ -t_{sz}^{(2)} g_2^\pm & \pm t_{xz}^{(2)} g_2^\pm & 0 & t_{zz}^{(2)} g_2^\pm \end{bmatrix}, \quad (\text{A4})$$

with

$$g_2^\pm(\mathbf{k}) = e^{i\mathbf{d}_2^\pm \cdot \mathbf{k}}; \quad (\text{A5})$$

$$\mathbf{T}_3 = \begin{bmatrix} t_{ss}^{(3)} g_3^+ & 0 & t_{sy}^{(3)} g_3^- & 0 \\ 0 & t_{xx}^{(3)} g_3^+ & 0 & 0 \\ -t_{sy}^{(3)} g_3^- & 0 & t_{yy}^{(3)} g_3^+ & 0 \\ 0 & 0 & 0 & t_{zz}^{(3)} g_3^+ \end{bmatrix}, \quad (\text{A6})$$

with

$$g_3^\pm(\mathbf{k}) = e^{i\mathbf{d}_3 \cdot \mathbf{k}} \pm e^{-i\mathbf{d}_3 \cdot \mathbf{k}}; \quad (\text{A7})$$

$$\mathbf{T}_4 = \begin{bmatrix} t_{ss}^{(4)} g_4^+ & t_{sx}^{(4)} g_4^+ & t_{sy}^{(4)} g_4^- & 0 \\ -t_{sx}^{(4)} g_4^+ & t_{xx}^{(4)} g_4^+ & t_{xy}^{(4)} g_4^- & 0 \\ -t_{sy}^{(4)} g_4^- & t_{xy}^{(4)} g_4^- & t_{yy}^{(4)} g_4^+ & 0 \\ 0 & 0 & 0 & t_{zz}^{(4)} g_4^+ \end{bmatrix}, \quad (\text{A8})$$

with

$$g_4^\pm(\mathbf{k}) = e^{i\mathbf{d}_4 \cdot \mathbf{k}} (1 \pm e^{-i\mathbf{a} \cdot \mathbf{k}}); \quad (\text{A9})$$

$$\mathbf{T}_5 = \begin{bmatrix} t_{ss}^{(5)} g_5^{+++} & t_{sx}^{(5)} g_5^{++-} & t_{sy}^{(5)} g_5^{+-+} & t_{sz}^{(5)} g_5^{+++} \\ -t_{sx}^{(5)} g_5^{++-} & t_{xx}^{(5)} g_5^{+++} & t_{xy}^{(5)} g_5^{---} & t_{xz}^{(5)} g_5^{++-} \\ -t_{sy}^{(5)} g_5^{+-+} & t_{xy}^{(5)} g_5^{---} & t_{yy}^{(5)} g_5^{+++} & t_{yz}^{(5)} g_5^{+-+} \\ -t_{sz}^{(5)} g_5^{+++} & t_{xz}^{(5)} g_5^{++-} & t_{yz}^{(5)} g_5^{+-+} & t_{zz}^{(5)} g_5^{+++} \end{bmatrix}, \quad (\text{A10})$$

with

$$\begin{aligned} g_5^{+++}(\mathbf{k}) &= e^{i\mathbf{d}_5 \cdot \mathbf{k}} [1 + e^{-i\mathbf{a} \cdot \mathbf{k}} + e^{-i\mathbf{c} \cdot \mathbf{k}} (1 + e^{-i\mathbf{a} \cdot \mathbf{k}})] \\ g_5^{++-}(\mathbf{k}) &= e^{i\mathbf{d}_5 \cdot \mathbf{k}} [1 + e^{-i\mathbf{a} \cdot \mathbf{k}} - e^{-i\mathbf{c} \cdot \mathbf{k}} (1 + e^{-i\mathbf{a} \cdot \mathbf{k}})] \\ g_5^{+-+}(\mathbf{k}) &= e^{i\mathbf{d}_5 \cdot \mathbf{k}} [1 - e^{-i\mathbf{a} \cdot \mathbf{k}} + e^{-i\mathbf{c} \cdot \mathbf{k}} (1 - e^{-i\mathbf{a} \cdot \mathbf{k}})] \\ g_5^{---}(\mathbf{k}) &= e^{i\mathbf{d}_5 \cdot \mathbf{k}} [1 - e^{-i\mathbf{a} \cdot \mathbf{k}} - e^{-i\mathbf{c} \cdot \mathbf{k}} (1 - e^{-i\mathbf{a} \cdot \mathbf{k}})] \end{aligned} \quad (\text{A11})$$

$$\mathbf{T}_6^R = \begin{bmatrix} t_{ss}^{(6)} g_{6R}^+ & t_{sx}^{(6)} g_{6R}^+ & t_{sy}^{(6)} g_{6R}^- & t_{sz}^{(6)} g_{6R}^+ \\ -t_{sx}^{(6)} g_{6R}^+ & t_{xx}^{(6)} g_{6R}^+ & t_{xy}^{(6)} g_{6R}^- & t_{xz}^{(6)} g_{6R}^+ \\ -t_{sy}^{(6)} g_{6R}^- & t_{xy}^{(6)} g_{6R}^- & t_{yy}^{(6)} g_{6R}^+ & t_{yz}^{(6)} g_{6R}^- \\ -t_{sz}^{(6)} g_{6R}^+ & t_{xz}^{(6)} g_{6R}^+ & t_{yz}^{(6)} g_{6R}^- & t_{zz}^{(6)} g_{6R}^+ \end{bmatrix}, \quad (\text{A12})$$

with

$$g_{6R}^\pm(\mathbf{k}) = e^{i\mathbf{d}_{6R} \cdot \mathbf{k}} (1 \pm e^{-i2\mathbf{a} \cdot \mathbf{k}}); \quad (\text{A13})$$

$$\mathbf{T}_6^L = \begin{bmatrix} t_{ss}^{(6)} g_{6L}^+ & -t_{sx}^{(6)} g_{6L}^+ & t_{sy}^{(6)} g_{6L}^- & t_{sz}^{(6)} g_{6L}^+ \\ t_{sx}^{(6)} g_{6L}^+ & t_{xx}^{(6)} g_{6L}^+ & -t_{xy}^{(6)} g_{6L}^- & -t_{xz}^{(6)} g_{6L}^+ \\ -t_{sy}^{(6)} g_{6L}^- & -t_{xy}^{(6)} g_{6L}^- & t_{yy}^{(6)} g_{6L}^+ & t_{yz}^{(6)} g_{6L}^- \\ -t_{sz}^{(6)} g_{6L}^+ & -t_{xz}^{(6)} g_{6L}^+ & t_{yz}^{(6)} g_{6L}^- & t_{zz}^{(6)} g_{6L}^+ \end{bmatrix}, \quad (\text{A14})$$

with

$$g_{6L}^\pm(\mathbf{k}) = e^{i\mathbf{d}_{6L} \cdot \mathbf{k}} (1 \pm e^{-i2\mathbf{a} \cdot \mathbf{k}}); \quad (\text{A15})$$

$$\mathbf{T}_7^\pm = \begin{bmatrix} t_{ss}^{(7)} g_7^\pm & \pm t_{sx}^{(7)} g_7^\pm & 0 & t_{sz}^{(7)} g_7^\pm \\ \mp t_{sx}^{(7)} g_7^\pm & t_{xx}^{(7)} g_7^\pm & 0 & \pm t_{xz}^{(7)} g_7^\pm \\ 0 & 0 & t_{yy}^{(7)} g_7^\pm & 0 \\ -t_{sz}^{(7)} g_7^\pm & \pm t_{xz}^{(7)} g_7^\pm & 0 & t_{zz}^{(7)} g_7^\pm \end{bmatrix}, \quad (\text{A16})$$

with

$$g_7^\pm(\mathbf{k}) = e^{i\mathbf{d}_7^\pm \cdot \mathbf{k}}; \quad (\text{A17})$$

$$\mathbf{T}_8 = \begin{bmatrix} t_{ss}^{(8)} g_8^+ & t_{sx}^{(8)} g_8^- & 0 & 0 \\ -t_{sx}^{(8)} g_8^- & t_{xx}^{(8)} g_8^+ & 0 & 0 \\ 0 & 0 & t_{yy}^{(8)} g_8^+ & 0 \\ 0 & 0 & 0 & t_{zz}^{(8)} g_8^+ \end{bmatrix}, \quad (\text{A18})$$

with

$$g_8^\pm(\mathbf{k}) = e^{i\mathbf{d}_8 \cdot \mathbf{k}} \pm e^{-i\mathbf{d}_8 \cdot \mathbf{k}}. \quad (\text{A19})$$

In those relations, $\mathbf{t}_{ss}^i = V_{ss\sigma}(d_i)$, $\mathbf{t}_{\alpha\beta}^i = (d_i^\alpha d_i^\beta / (d_i)^2) V_{pp\sigma}(d_i) + (\delta_{\alpha\beta} - d_i^\alpha d_i^\beta / (d_i)^2) V_{pp\pi}(d_i)$ and $\mathbf{t}_{\alpha\gamma}^i = (d_i^\alpha / d_i) V_{sp\sigma}(d_i)$, where $\mathbf{d}_i = (d_i^x, d_i^y, d_i^z)$ and $d_i = |\mathbf{d}_i|$. The indices run as follows: $i = 1, \dots, 8$ and $\alpha, \beta = x, y, z$. The phase factors g_i are defined as function of the distances and the wave number \mathbf{k} .

These definitions are similar to those used in the previous models in the literature,¹⁶ with the addition of new interatomic matrix elements T_3 , T_4 , T_5 , T_6 , T_7 , and T_8 . The reason for introducing these new parameters is that the two interatomic matrix elements T_1 and T_2 provided by the Slater-Koster coefficients are not sufficient to accurately describe the band structure of phosphorene. These must be modified in order to provide an accurate representation of the band gap. By diagonalizing H , the band dispersion of monolayer phosphorus can be obtained, as shown in Fig. 2.

¹ A. H. Castro Neto, F. Guinea, N. M. R. Peres, K. S. Novoselov, and A. K. Geim, *Rev. Mod. Phys.* **81**, 109

- ² W. Xie and Z. Li, *Solid State Communications* **225**, 22 (2016).
- ³ L. Li, Y. Yu, G. J. Ye, Q. Ge, X. Ou, H. Wu, D. Feng, X. H. Chen, and Y. Zhang, *Nat Nano* **9**, 372 (2014).
- ⁴ H. Liu, A. T. Neal, Z. Zhu, Z. Luo, X. Xu, D. Tománek, and P. D. Ye, *ACS Nano* **8**, 4033 (2014).
- ⁵ A. Mishchenko, Y. Cao, G. L. Yu, C. R. Woods, R. V. Gorbachev, K. S. Novoselov, A. K. Geim, and L. S. Levitov, *Nano Letters* **15**, 6991 (2015).
- ⁶ F. Xia, H. Wang, and Y. Jia, *Nat Commun* **5**, 4458 (2014).
- ⁷ Y. Liu, T. Low, and P. P. Ruden, *Phys. Rev. B* **93**, 165402 (2016).
- ⁸ Y. Takao, H. Asahina, and A. Morita, *Journal of the Physical Society of Japan* **50**, 3362 (1981).
- ⁹ A. S. Rodin, A. Carvalho, and A. H. Castro Neto, *Phys. Rev. Lett.* **112**, 176801 (2014).
- ¹⁰ T. Low, A. S. Rodin, A. Carvalho, Y. Jiang, H. Wang, F. Xia, and A. H. Castro Neto, *Phys. Rev. B* **90**, 075434 (2014).
- ¹¹ J. Paier, M. Marsman, K. Hummer, G. Kresse, I. C. Gerber, and J. G. ngyn, *The Journal of Chemical Physics* **124**, 154709 (2006).
- ¹² A. N. Rudenko, S. Yuan, and M. I. Katsnelson, *Phys. Rev. B* **92**, 085419 (2015).
- ¹³ S. Yuan, A. N. Rudenko, and M. I. Katsnelson, *Phys. Rev. B* **91**, 115436 (2015).
- ¹⁴ E. Taghizadeh Sisakht, M. H. Zare, and F. Fazileh, *Phys. Rev. B* **91**, 085409 (2015).
- ¹⁵ Z. S. Popović, J. M. Kurdestany, and S. Satpathy, *Phys. Rev. B* **92**, 035135 (2015).
- ¹⁶ T. Osada, *Journal of the Physical Society of Japan* **84**, 013703 (2015).
- ¹⁷ J. Heyd, G. E. Scuseria, and M. Ernzerhof, *The Journal of Chemical Physics* **118**, 8207 (2003).
- ¹⁸ J. Heyd, G. E. Scuseria, and M. Ernzerhof, *The Journal of Chemical Physics* **124**, 219906 (2006).
- ¹⁹ J. D. Wood, S. A. Wells, D. Jariwala, K.-S. Chen, E. Cho, V. K. Sangwan, X. Liu, L. J. Lauhon, T. J. Marks, and M. C. Hersam, *Nano Letters* **14**, 6964 (2014).
- ²⁰ J. O. Island, G. A. Steele, H. S. J. van der Zant, and A. Castellanos-Gomez, *2D Materials* **2**, 011002 (2015).
- ²¹ R. A. Doganov, E. C. T. O'Farrell, S. P. Koenig, Y. Yeo, A. Ziletti, A. Carvalho, D. K. Campbell, D. F. Coker, K. Watanabe, T. Taniguchi, A. H. C. Neto, and B. Ozyilmaz, *Nat Commun* **6** (2015).
- ²² W. Hu and J. Yang, *The Journal of Physical Chemistry C* **119**, 20474 (2015).
- ²³ Y. Liu, F. Xu, Z. Zhang, E. S. Penev, and B. I. Yakobson, *Nano Letters* **14**, 6782 (2014).
- ²⁴ A. Ziletti, A. Carvalho, D. K. Campbell, D. F. Coker, and A. H. Castro Neto, *Phys. Rev. Lett.* **114**, 046801 (2015).
- ²⁵ V. V. Kulish, O. I. Malyi, C. Persson, and P. Wu, *Phys. Chem. Chem. Phys.* **17**, 992 (2015).
- ²⁶ P. Li and I. Appelbaum, *Phys. Rev. B* **90**, 115439 (2014).
- ²⁷ J. C. Slater and G. F. Koster, *Phys. Rev.* **94**, 1498 (1954).
- ²⁸ P. E. Blöchl, *Phys. Rev. B* **50**, 17953 (1994).
- ²⁹ G. Kresse and D. Joubert, *Phys. Rev. B* **59**, 1758 (1999).
- ³⁰ G. Kresse and J. Furthmüller, *Phys. Rev. B* **54**, 11169 (1996).
- ³¹ G. Kresse and J. Hafner, *Phys. Rev. B* **47**, 558 (1993).
- ³² A. Brown and S. Rundqvist, *Acta Crystallographica* **19**, 684 (1965).
- ³³ J. Qiao, X. Kong, Z.-X. Hu, F. Yang, and W. Ji, *Nat Commun* **5**, 4475 (2014).
- ³⁴ S. Das, W. Zhang, M. Demarteau, A. Hoffmann, M. Dubey, and A. Roelofs, *Nano Letters* **14**, 5733 (2014).
- ³⁵ X. Wang, A. M. Jones, K. L. Seyler, V. Tran, Y. Jia, H. Zhao, H. Wang, L. Yang, X. Xu, and F. Xia, *Nat Nano* **10**, 517 (2015).
- ³⁶ E. Ridolfi, D. Le, T. S. Rahman, E. R. Mucciolo, and C. H. Lewenkopf, *Journal of Physics: Condensed Matter* **27**, 365501 (2015).
- ³⁷ Z. Zhu and D. Tománek, *Phys. Rev. Lett.* **112**, 176802 (2014).
- ³⁸ A. N. Rudenko and M. I. Katsnelson, *Phys. Rev. B* **89**, 201408 (2014).
- ³⁹ J. Lee, J. Seo, J. H. Oh, and M. Shin, *Nanotechnology* **27**, 245202 (2016).
- ⁴⁰ J. Chang and C. Hobbs, *Applied Physics Letters* **106**, 083509 (2015).
- ⁴¹ S. R. Suryawanshi, M. A. More, and D. J. Late, *Journal of Vacuum Science Technology B* **34**, 041803 (2016).
- ⁴² R. Fei and L. Yang, *Nano Letters* **14**, 2884 (2014).
- ⁴³ A. Ferreira and E. R. Mucciolo, *Phys. Rev. Lett.* **115**, 106601 (2015).
- ⁴⁴ W. A. Harrison, *Electronic Structure and the Properties of Solids: The Physics of the Chemical Bond*, Dover ed. (New York, 1989).
- ⁴⁵ C. Caroli, R. Combescot, D. Lederer, P. Nozieres, and D. Saint-James, *Journal of Physics C: Solid State Physics* **4**, 2598 (1971).
- ⁴⁶ C. H. Lewenkopf and E. R. Mucciolo, *Journal of Computational Electronics* **12**, 203 (2013).
- ⁴⁷ M. P. L. Sancho, J. M. L. Sancho, J. M. L. Sancho, and J. Rubio, *Journal of Physics F: Metal Physics* **15**, 851 (1985).
- ⁴⁸ P. A. Lee and D. S. Fisher, *Phys. Rev. Lett.* **47**, 882 (1981).
- ⁴⁹ A. Rycerz, J. Tworzydo, and C. W. J. Beenakker, *EPL (Europhysics Letters)* **79**, 57003 (2007).
- ⁵⁰ S. Narita, Y. Akahama, Y. Tsukiyama, K. Muro, S. Mori, S. Endo, M. Taniguchi, M. Seki, S. Suga, A. Mikuni, and H. Kanzaki, *Physica B+C* **117**, 422 (1983).
- ⁵¹ Y. Akahama, S. Endo, and S. ichiro Narita, *Journal of the Physical Society of Japan* **52**, 2148 (1983).